Room temperature and high pressure-pulsed laser deposited of nanocrystalline VO_2 thin films on glass substrate: plasma and films analyses

Slimane Lafane[1], Smail Malek[1], Jackie Nel[2], Samira Abdelli-Messaci[1]

[1]Division des Milieux Ionisés et Laser, Centre de Développement des Technologies Avancées, Cité du 20 août 1956, B. P. 17, Baba Hassen, Algiers, Algeria.

[2]Physics department, University of Pretoria, Lynnwood Road, Pretoria, South Africa.

Corresponding author: slafane@cdta.dz

Abstract

In this contribution, we demonstrate room temperature growth of highly oriented single phase nanocrystalline films of VO_2(A) on glass substrates using pulsed laser deposition (PLD) technique under high oxygen pressure and small target-substrate separation. The structural, morphological, optical, electrical and compositional properties of the deposited thin films have been studied by means of X-ray diffraction, atomic force microscopy, spectrophotometry, 04 probe method and X-ray photoelectron spectroscopy, respectively. The plasma under which VO_2(A) was grown has been analyzed by means of time- and space-resolved optical emission spectroscopy (OES) and Langmuir probe (LP) techniques. We evidenced a correlation between growth conditions and plasma characteristics. While OES showed that at the deposition distance corresponding to the length of the visible plasma, the plasma species are completely thermalized and characterized by a very low degree of excitation, LP technique indicated a formation of charged clusters within the gas phase. By combining OES and LP data, a quadruple plasma structure has been shown. The growth of under-stoichiometric (comparing to the parent V_2O_5 target) nanocrystalline VO_2(A) phase has been attributed to nanoparticles formation in the gas phase under a plasma environment rarefied in oxygen atoms due to the scattering and backscattering effects. This finding opens

up the opportunity to grow VO_2 polymorphs at very low temperature by PLD for novel promising new device functionalities.

Keywords: pulsed laser deposition, nanocrystalline vanadium dioxide, room temperature, high oxygen pressure, plasma diagnostics.

1. Introduction

Thin films of vanadium dioxide have been considered of great interest due to their exceptional semiconductor-to-metal transition characteristics [1]. This is motivated by numerous applications when integrating vanadium dioxide thin films in phase change based technological applications such as micro-optical switch device [2], energy conservation and energy storage [3] and novel electronics, photonics, and related devices [4] . VO_2 has multiple polymorphic forms with four major phases called R, M, A and B-phases [3]. Although, the most attractive and studied phase which motivated the interest of scientists is VO_2(M) phase in relation to its transition to VO_2(R) close to the ambient temperature, metastable VO_2(A) emerge to have also drawn considerable attention [5] for its novel suggested potential applications and novel fundamentals properties [6-11].

In recent years, few works on lower temperature deposition of VO_2 can be found [12]. Generally, regardless of the physical methods used and the polymorph phase, high temperatures in the range of 400 to 500°C are required to grow crystalline vanadium dioxide thin films [9, 11, 13-16]. However, efforts have been made to reduce the synthesis temperature, particularly for VO_2(M) phase, for applications necessitating a deposit on flexible substrates [17-19] and as multilayer films [20, 21], for thermochromic, optoelectronic and microelectronic functional device fabrication. Due to the temperature-sensitivity for the former case and the interfacial diffusion with the formation of undesirable compound in the latter case, lowering the temperature at which the devices are made is required [22]. Growth

temperatures around 300°C have been reported [17-20, 22-26]**.** Among those latter references, only Soltani *et al.* [19] employed pulsed laser deposition (PLD) method, in its conventional format (nanosecond (ns) PLD). Despite this still limited interest on low temperature PLD of VO_2, among all fabrication techniques, only ns PLD has shown to be efficient to grow VO_2 (M phase) thin films at room temperature without post-annealing. This was achieved by Maaza *et al.* [27]. Conversely, femtosecond (fs) PLD, from the only study available up today, has produced crystalline vanadium dioxide films when the deposition is carried out at elevated temperature [28]. This could be due to the fact that oxides that have been deposited by fs PLD often showed a low degree of crystallinity comparing to ns PLD [29].

The ns PLD is known to produce crystalline oxide thin films at room temperature [16, 30-33] through two distinct ways, either, under vacuum or very low pressure, by taking advantage of the high kinetic energy of the ablated species within the plasma [31, 33] to compensate the thermally activated adatoms mobility on the substrate surface or at high gas pressure to form nanocrystalline particles in the gas phase to be deposited as nanocrystalline thin films [30, 32, 34-36]. To date, very little is known about ns PLD synthesis of crystalline vanadium dioxide thin films at room temperature and the related plasma dynamics remains unexplored. This was the initial motivation for the present work. The second motivation is the great demand of the synthesis of VO_2 polymorphs nanoparticles [37]. In this context, nanoparticles assembled thin films synthesized by ns PLD have unique physical properties [38] that could lead to superior VO_2 based device performances.

Here, we employed high pressure ns PLD to explore room temperature deposition of nanocrystalline vanadium dioxide thin films and to investigate the related plasma conditions. Our results demonstrate the feasibility to grow highly oriented nanocrystalline vanadium dioxide VO_2(A) thin films at room temperature and provide key information on the plasma properties that define the mechanisms behind this achievement. This will, in future, allow the

selective growth of vanadium dioxide polymorphs using particular conditions of the plasma at high oxygen pressures.

2. Experimental

The plasma for thin films deposition was produced by pulsed laser ablation of a homemade V_2O_5 rotating target [39] using a KrF laser (λ = 248 nm, τ = 25 ns). As previously described [39], the plasma was analyzed by time- and space-resolved optical emission spectroscopy (OES) and Langmuir probe (LP) techniques. By plasma imaging and horizontally translating onto 100 µm entrance slit of an Acton spectrometer, spatially resolved of the optical emission of the plasma species was obtained. Coupled to a spectrometer and connected to a digital oscilloscope (Tektronix DPO4054B), a fast Hamamatsu R928 photomultiplier provided the temporal resolved electrical signals generated by the plasma emission. In addition to OES technique, the plasma ions were studied by a cylindrical LP immersed into the plasma to record spatially and temporally resolved ionic currents. The LP was biased at −40 V and connected to the oscilloscope. The study has been done under 2 Jcm^{-2} of laser fluence and 5 mbar of oxygen pressure. The selection of this pressure is motivated by the fact that nanoparticles of a broad range of materials in PLD process are produced under a gas pressure in the range of 5 to 50 mbar [40]. For a practical distance of deposition, the lower limit of the pressure range was considered.

The thin films were grown on 1 cm × 1 cm Corning glass (1737) substrates at room temperature for 300 laser pulses using 5 Hz laser repetition rate and 1 min of deposition. Taking into account the plasma study, the substrate was set at a distance of 11 mm from the target surface. After the deposition, no post-annealing has been carried out. Under these conditions, the thickness of the deposited films was measured to be around 60 nm by surface profilometer given an effective deposition rate of ~ 0.2 nm/pulse. Grazing incidence X-ray diffraction (GIXRD) without K_β filtering (Bruker D8 Advance) and atomic force microscopy

(AFM) (Bruker Scan Asyst) have been used for microstructural properties. The optical transmittance and reflectance measurements were carried out using a Cary 500 UV-vis-NIR spectrophotometer. The electrical measurements were done using a four probe method with an integrated heating stage and a source meter (Keithley 2400C). In order to examine the ionic state of vanadium ions, X-ray photoelectron spectroscopy (XPS) measurements were performed using Thermo Scientific ESCALAB Xi^{+}XPS Microprobe. High-resolution spectrum was recorded with 0.1 eV energy step, dwell time of 400 ms and an analyzer pass energy of 20 eV.

3. Results and discussion

3.1 Plasma analysis

Figure 1a shows typical time of flight (TOF) signals obtained by the photomultiplier. As we have already reported for a laser induced V_2O_5 plasma in vacuum [39], at 2 Jcm^{-2} we have observed the emission of VI (437.92 nm), VII (326.77 nm), VIII (237.10 nm), VIV (226.82 nm) and OI (777.19 nm) (more details about the selected atomic spectral lines can be found in [39]). We notice the presence of a continuum emission that appears at an unchanged time delay independently of the plasma displacement. This emission is not considered. By recording TOF signals at different distances from the target surface (see Fig. 1b for typical signals), we had access to temporally and spatially resolved plasma species emission and dynamics. The distance from the target surface as a function of the time delay for the most of the plasma species (maximum emission) and for the fast plasma species (considered at 10% of the maximum emission) are given in Fig. 2a and 2b. First of all, due to the high plasma confinement, the plasma species spatio-temporal trajectory doesn't exhibit important dependence on their mass or charge. Their expansion follows a distance-time relation predicted by Predteceensky and Mayorov (PM) model [41-43] (see Fig. 2a and 2b) which is

based on the balance between linear momentum variation and the external pressure force giving the plasma velocity u and position R through the governing equation:

$$\frac{d}{dt}\left[\left(M_p + M_g(R)\right)u\right] = -2\pi R^2 P_g$$

where M_p is the confined plasma mass. P_g and $M_g = 2/3\pi\rho_g R^3$ (ρ_g being the background gas density) are the background gas pressure and the swept-up mass.

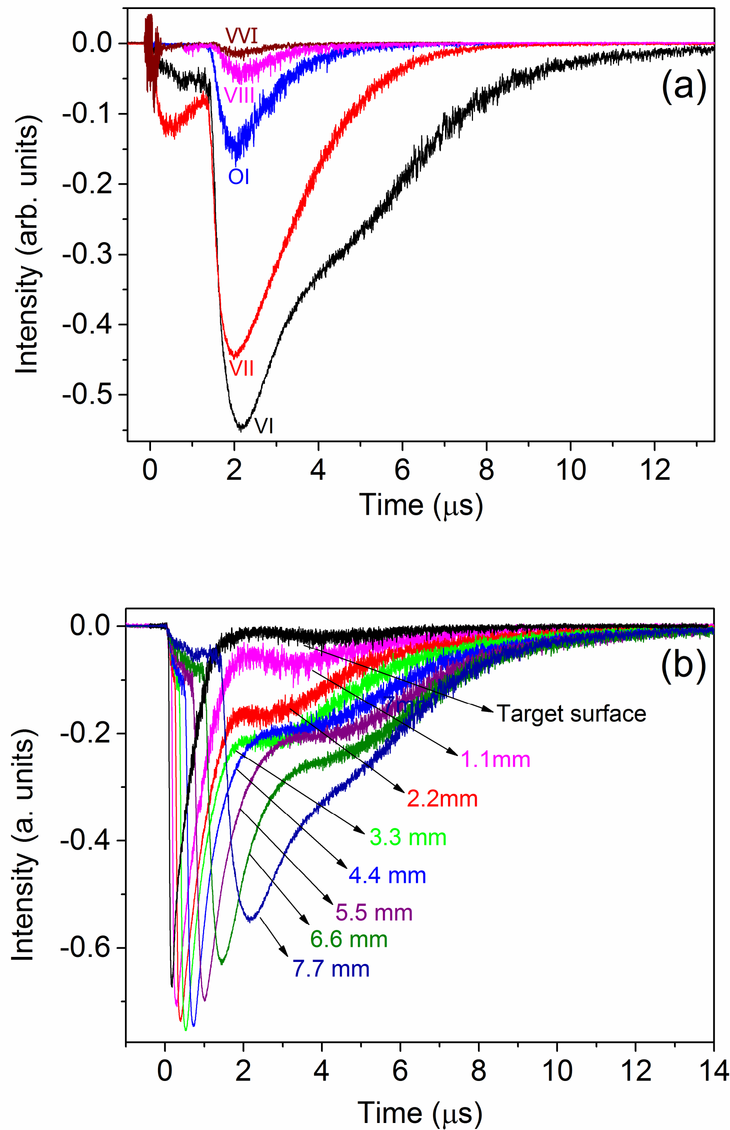

Fig. 1 a Typical TOF signals of VI, VII, VIII, VIV and OI emission recorded at 7.7 mm. The intensity of OI, VIII and VIV are multiplied by a factor of 2, 10 and 20, respectively. **b** Typical TOF signals of neutral vanadium (VI) emission recorded at different distances.

PM model provides a clear and general description of the plasma species propagation into the oxygen gas. Initially, the plasma species propagates with vacuum-like behavior over a very short distance and starts to follow a dynamic regime where the plasma species slows down due to the combined influence of gas accumulated at the contact front and the force exerted by the background gas pressure [43]. The data obtained by PM model enabled us to determine the average and the maximum velocities of the plasma species and then their kinetic energy (K_E) throughout their flight to the distance of deposit (Fig. 2c). As can be seen in Fig. 2c, K_E drops sharply with increasing the distance from the target. Near the target surface, the maximum kinetic energy for the vanadium species is 45 eV, and this drops to 0.17 eV at a distance of 11 mm from the target. For more details, we present K_E of all the plasma species near the target surface and at a distance of 11 mm from the surface in Table 1. It can be concluded that the plasma species arrive completely thermalized at this distance.

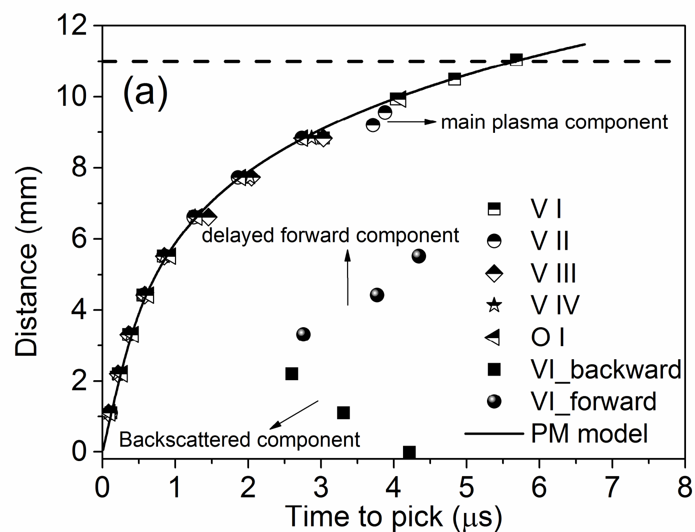

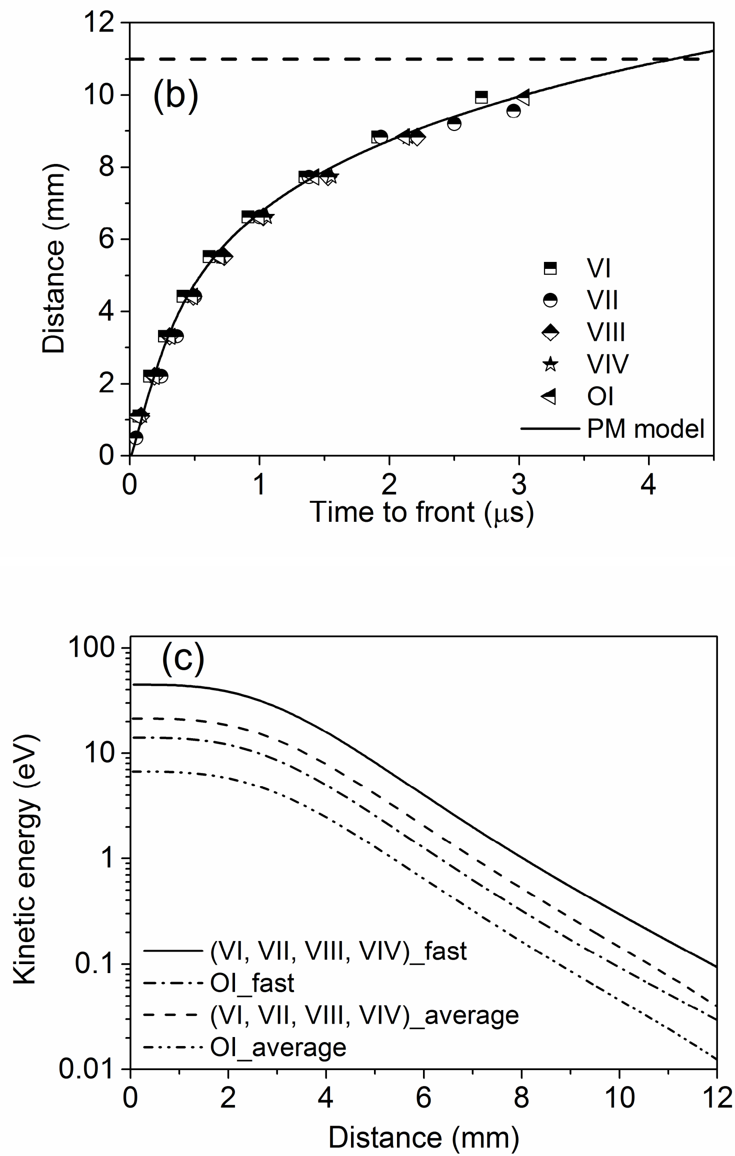

Fig. 2 Distance-time plots of the plasma species, **a** maximum population and **b** fast population. The horizontal dashed line is an aid to the eye to show the deposition distance. **c** Kinetic energy of plasma species versus the distance from the target surface. Average and fast in the graph concern the K_E of the most and fast plasma species, respectively.

Table 1 Average and maximum energies of plasma species at the target surface and at a distance of 11 mm.

Plasma species	Average K_E near target surface (eV)	Average K_E at 11 mm (eV)	Maximum K_E near target surface (eV)	Maximum K_E at 11mm (eV)
Vanadium (ions and neutrals)	21.5	0.08	45	0.17
Oxygen (neutral)	6.7	0.025	14	0.05

In addition to the plasma kinetic energy, the plasma internal energy, represented qualitatively by the energy involved in the plasma species excitation/emission, is of a great interest in thin films deposition process [44]. Figure 3 shows the maximum emission intensity of neutral species V and O, and ionized species V^+. An interesting observation in Fig. 3 is that there are two distinct regions. The first region before 5mm where the maximum emission intensity is increased. The second region beyond 5 mm is characterized by a sharp drop of the emission intensity. The increase in the maximum emission intensity of the plasma species in the first region is due to the substantial accumulation and heating of the plasma in the shocked gas region [45]. It is well known that with sufficient background gas pressure, the interplay between plasma species and gas molecules results in shock wave formation in the plasma front-gas interface which tends to increase both the amount of ablated species and its excitation degree [46]. This starts from the initial expansion of the plasma due to the high

oxygen pressure used here. At a distance of 11 mm, the plasma species emission intensity reaches a very low level (the plasma is almost completely extinguished).

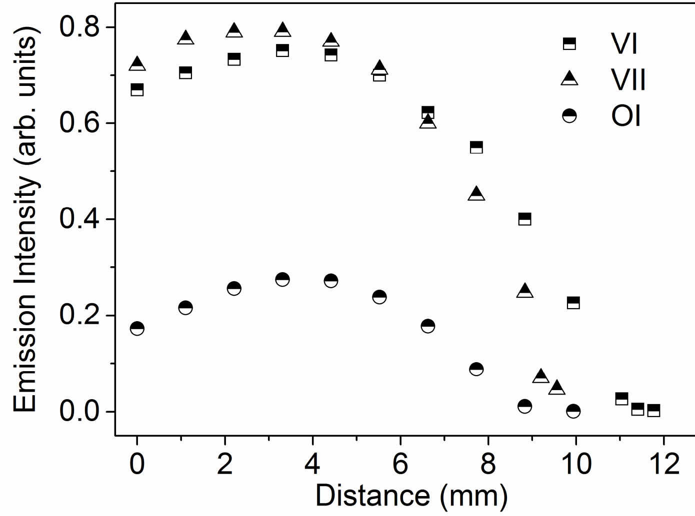

Fig. 3 Maximum emission intensity of VI, VII and OI versus the distance from the target surface

In order to give more insight into the observed drop of the plasma emission intensity, we analyzed the distance travelled by the plasma front using the analytical shock-wave model where the time evolution of the shock front position depends on the plasma expansion symmetry [42]. In Fig. 4, it is clearly seen that initially the plasma expansion symmetry is planar ($d \sim t^{2/3}$), and this later changes to hemi-spherical, following the power law ($d \sim t^{2/5}$). The distance from which the plasma expansion symmetry passes from planar to hemi-spherical, i.e., the plasma passes from highly forward peaked to more homogenous expansion, coincides with the distance where the plasma emission drops, i.e., ~ 5mm. This symmetry transition leads to larger volume evolution of the plasma. Consequently, the plasma internal energy spreads over this larger volume, reducing by this way the plasma emission intensity. Further, due to the observed plasma clustering (this will be discussed further below), plasma species coalesced and this led to the reduction of the number of emitting plasma species that could contribute to the drop of plasma emission.

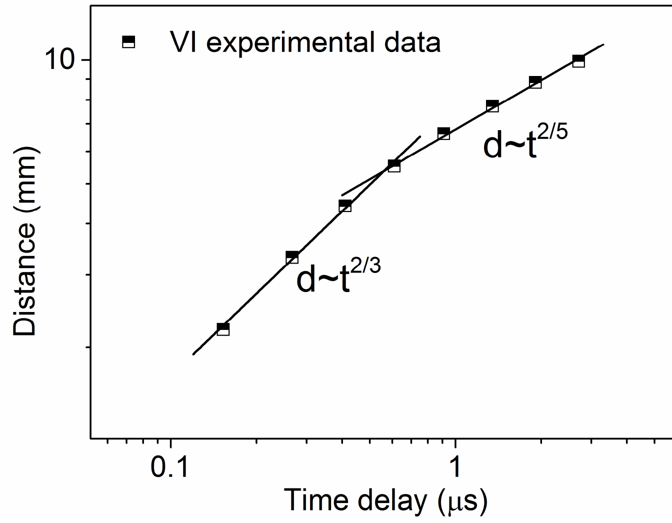

Fig. 4 Distance-time plot analyzed through shock-wave model using VI data.

A secondary vanadium and oxygen species component is observed up to a distance of 7.7 mm for neutral vanadium (VI) (see Fig. 1 for VI). Neutral oxygen (OI) and ionized vanadium (VII) were observed in a very limited region around 2 mm at a time delay of 2.6 μs (Fig. 5). We think that is due to the high energy involved in excitation and ionization of those two species in contrary to neutral vanadium atoms [39].

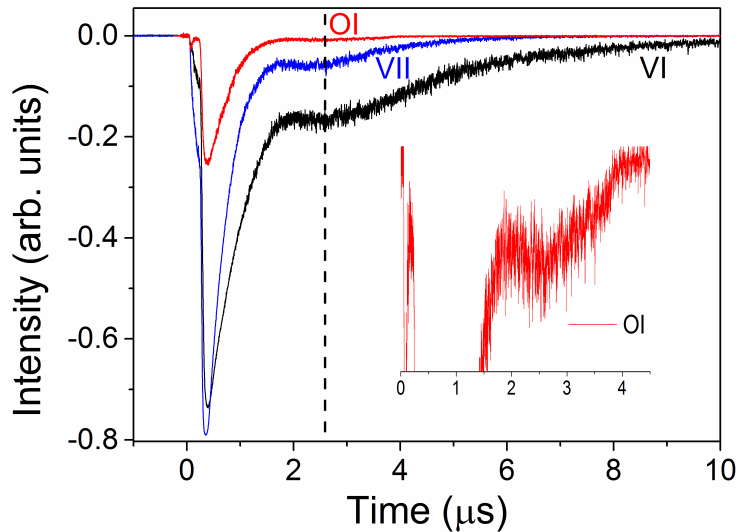

Fig. 5 Typical TOF signals of VI, VII and OI emission of the main plasma and backscattered components recorded at 2.2 mm. The dashed vertical line shows the appearance time of the backscattered components. Inset: the emission signal of the backscattered oxygen (OI).

From VI data presented in Fig. 1b, we highlight the temporal profile of the secondary VI component for typical distances in Fig. 6. From figures 6 and 1b, we distinguish two secondary components, one is moving backwards and the other is moving forwards with largely delayed time. While the backscattered component reaches the target surface at 4.2 µs, the delayed one reaches a distance of 5.5 mm and the main plasma component arrives at 10 mm. This clearly reveals the internal triple structure of the plasma as reported by Yousfi *et al.* [47] for an expanding Carbon plasma under relatively high argon pressure. The plasma components which move back and forth probably consist of atoms which first backscattered from the plasma when colliding with oxygen molecules, then interact with the incoming slower plasma species to form a secondary delayed component [48] or diffuse to reach the target surface. Our observations support strongly the backscattering mechanism involved in the formation of the delayed plasma component as suggested by Canulescu *et al.* [48], Amoruso *et al.* [49] and Itina *et al.* [50] through, respectively, their OES, fast imaging and Monte Carlo simulation data.

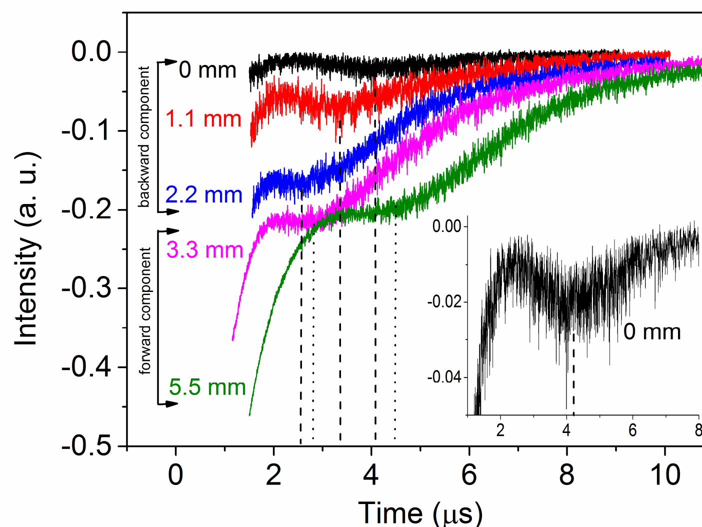

Fig. 6 Typical TOF signals of the secondary VI component. The dashed and the dotted lines show the appearance time of the backward and forward moving components. Inset: backwards moving component recorded near the target surface.

For additional information about ionized species, we collected ionic TOF signals by setting the Langmuir probe at 11 mm (Fig. 7). The fast narrow peak at almost zero time is due to photoelectrons emission from the metal of the probe tip induced by scattered laser photons and UV photons from the plume [51]. Three distinct peaks were observed corresponding to three populations of ionic species. Using a LP, a complex three modal distribution of plasma ions was observed in laser induced plasma of different materials [52, 53]. Generally, the fast population was considered to be those ions that have suffered almost no collisions with the oxygen particles [43, 52, 53]. If one considers the initial plasma velocity (0.9×10^6 cm/s from Fig. 2a), the arrival time of the fast ions should be 1.2 µs which is lower than that of the present case (2µs). Further, using oxygen gas, the fast ion population has been commonly observed for pressures less than 1 mbar [54-56]. For a higher pressure as used in this study, these ion populations are completely transferred to the main delayed plasma component through multiple-scattering process [57]. Considering the analysis provided by Wood *et al.* [58] and the collisions laws given in [59], if one considers the case of head-on elastic collisions between the heavier plasma species (vanadium atoms) and ambient oxygen molecules, the latter should have a velocity greater than that of vanadium species (neutral and ions). This suggests that if oxygen molecules were ionized, the LP would detect them at an earlier time delay. From the OES study, the plasma expansion is planar over half the path way before arriving at the LP, which suggests that head-on collisions between plasma species and oxygen molecules are effective. Further, considering the ionization potential of oxygen molecules (12 eV) [60] and the internal and kinetic energies (up to 45 eV) available in the plasma, it would be possible to ionize oxygen molecules. Further, including the ionized oxygen molecules into the fast ions observed by the LP would be feasible.

The second population represents ions that have been slowed down by collisions with oxygen molecules. Their time of arrival (3.9 µs) to the LP match well with that of the leading

edge of the plasma observed by OES (~ 4 μs). In view of its very late arrival time (around 14 μs), the third population represents very slow-moving ions indicating cluster formation through condensation of plasma species by means of gas-phase collision [52, 53, 61]. Effectively under such a high gas pressure, a part of the primary flux of atoms and ions changes to include small clusters and eventually, significant numbers of nanocrystals [52]. The supersaturation, the plasma temperature and ionization play a dominant role in the formation of clusters in laser ablation plumes. At high gas pressure, a large number of atoms are available in a very small volume due the high plasma confinement leading to a very high plasma density. Jointly with the rapid lowering of the plasma temperature (quenching effect) [62] this will result in attaining a high degree of supersaturation driving to the plasma species to condensate, to produce clusters and nanoparticles by further collision-aggregation of clusters. Further, according to Tillack *et al.* [61] in addition to the supersaturation effect, ionized clusters are produced through ion-induced nucleation mechanisms. It was reported that charged ions tend to be jacketed by surrounding neutral atoms leading to a high homogeneous nucleation rate [61]. This is effective in our case, since at the fluence used here (2 Jcm^{-2}), the V_2O_5 plasma has already reached its higher degree of ionization [39].

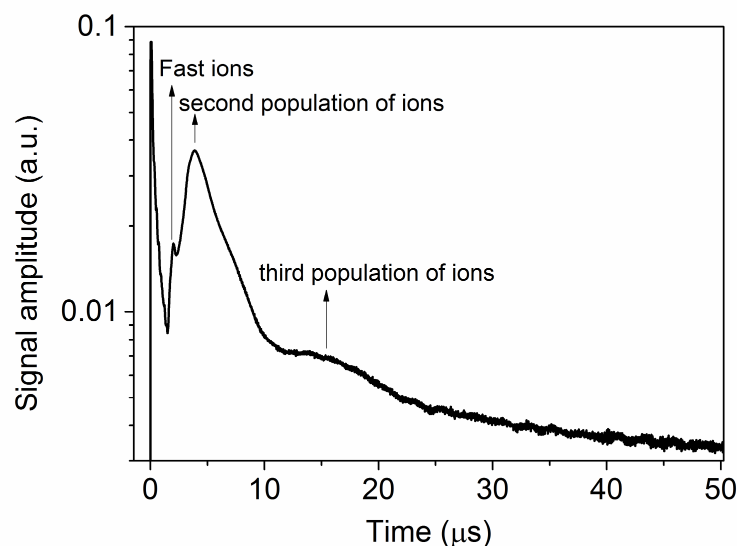

Fig. 7 Ion current versus time collected at a distance of 11 mm as measured by the LP.

For thin films deposition, we selected a distance of 11 mm. As generally known in PLD processes, the oxygen pressure and target-to-substrate distance are not independent parameters [63]. High quality oxide thin films grown in an oxygen environment match with the distance between the target and the substrate equivalent to the length of the visible plasma, i.e., where the kinetic energy of ablated species has been completely dissipated [64, 65]. This is motivated by the oxygen [64] and the microstructure (low roughness, dense morphology, high crystallinity) [53, 66, 67] adjustment and thereby the physical properties of the thin films [64, 66]. Furthermore, nanoparticles formation in the gas phase that lead to nanocrystalline films depends on the target-substrate separation. At high gas pressure (> 1mbar, few mbar), nanoparticles are rather formed near the plasma luminous length, when the plume energy is largely dissipated [68, 69]. In our case, all those plasma conditions are closely fulfilled at the indicated distance of 11 mm.

3.2 Thin films analysis

3.2.1 Structural properties

The X-ray diffraction pattern (background subtracted) of the deposited thin films and the normalized substrate and films XRD patterns are displayed in Fig. 8. Firstly, the figure shows that the deposited films are mainly crystalline (no obvious of any amorphous component). The XRD films pattern resembles to that presented in a previous report [9] where a (220) oriented tetragonal VO_2(A) with the dominant peak at 29.62° (29.5 ° in our case) has been reported (in agreement with JCPDS card No. 80-0690). This also adheres to what was reported by Ji *et al.* [70] where VO_2(A) nanorods were preferentially grown along [110] plane direction. Noting that (110) reflection which should be actually the strongest diffraction line is missing here as in [9], even if an elemental compositional analysis showed VO_2 stoichiometry. This feature has also been observed for other tetragonal material where the dominant (220) reflection line has been attributed to the short-range crystalline order [71].

VO_2(A) is highly oriented and shows a high crystalline quality (FWHM = 0.13°). The average out-of-plane crystallite size of the deposited films was calculated to be 67 nm using Scherrer's formula ($D = 0.9\lambda/\beta \cos \theta$), where D is the crystal size, λ is the wavelength of X-ray, θ is the Braggs angle, and β is the full width at half maximum of the peak [72]. We notice that while in our case, we stabilize a VO_2(A) single phase at room temperature and on amorphous glass substrate, in Srivastava *et al.* [9] work, VO_2(A) thin films have been epitaxially grown on $SrTiO_3$ single crystal at high substrate temperature (500°C). This is also the case of Lee *et al.* work [11], where VO_2(A) has been grown by pulsed laser epitaxy PLE on selective perovskite oxides single crystals at ~ 400 °C.

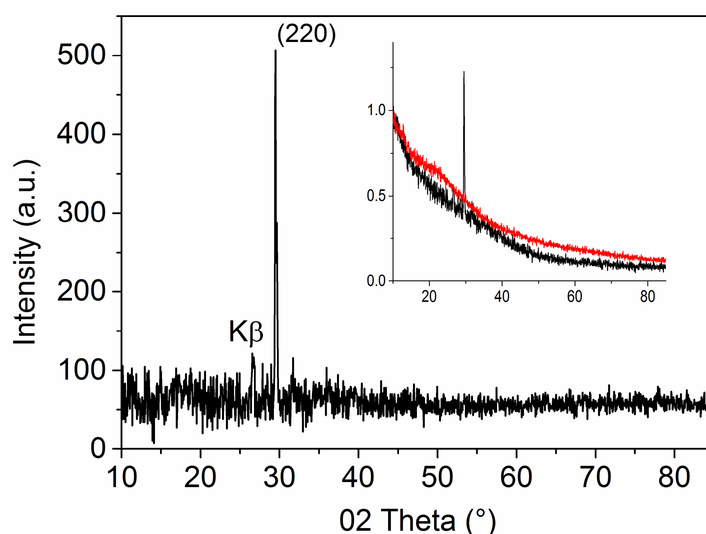

Fig. 8 XRD pattern of VO_2(A) thin films after background subtraction. Inset: normalized substrate and film XRD patterns to the maximum of background noise.

Generally, in addition to the substrate temperature, it was reported that plasma conditions such as the kinetic and the internal energy (the excitation state) of impinging species on the substrate play a significant role in influencing the PLD growth process of complex oxides [44, 46]. According to the plasma study presented above, the kinetic and internal energy of the plasma species are significantly reduced. This allows the assumption that the contribution of the plasma internal and kinetic energy to the nucleation and growth

process on the substrate surface is unimportant. Thus, the latter process should be considered in the gas phase [34]. The formation of clusters during plasma expansion observed by means of the LP clearly shows the possibility of the gas-phase synthesis of nanocrystalline vanadium oxide particles (nanoparticles). Those nanoparticles are condensed onto the substrate to form the crystalline thin film.

Concerning the crystallinity of the nanoparticles, this is related to the available thermal energy (plasma temperature) at the position in the plume where they grow. Considering the good agreement between our experimental data and the shock wave model predictions presented above, an estimate of this temperature can be made considering a strong shock conditions in the region of plasma-oxygen gas interface [73]. Accordingly, the following relation was used:

$$T_s = \frac{2\gamma}{(\gamma+1)}\left[\frac{(\gamma-1)}{(\gamma+1)}M^2 + 1\right]T_0$$

where T_s is the temperature of the shocked region, γ is the specific heats ratio (γ ~ 1.2 [73]), $M = v/c_s$ is the Mach number related to the sound velocity in oxygen ambient (c_s = 317.5 m/s at room temperature [74]) and to plasma species velocity deduced from the above plasma front position-time plots; T_0 is the temperature of the undisturbed gas (taken as room temperature). In the late stage of expansion corresponding to the plume length, T_s decreases down from thousands degrees to a value of several hundred degrees (~ 500°C). Even if this latter is given as an approximate indication, such temperature value is high enough to ensure crystallization, stabilization, preferential orientation and even a heterogeneous growth of the nanoparticles. Furthermore, the growth of a pure single phase indicates that the nanoparticles are grown in homogenous plasma region in terms of temperature and elemental composition. This supports the fact that stable nanoparticles formation occurs at a limited distance range, probably at the later stage of expansion of the plume as previously reported in a few reports [68, 69].

The growth of under-stoichiometric VO_2(A) phase compared to the stoichiometry of V_2O_5 parent target indicates a non-stoichiometric transfer of the target elements to the substrate. This can be explained as follows. It has been reported that from the same target composition, a wide range of film composition could be obtained [75]. In our case, three main processes could be responsible for the obtained oxygen poor films, incongruent ablation, collisions induced scattering and backscattering of the plasma species. The former process is valid when the laser fluence is around the ablation threshold [65]. The fluence (2Jcm^{-2}) used for the present study is, however, much higher compared to the ablation threshold (~ 0.3 Jcm^{-2}), previously reported [39]. Thus, we consider hereafter the two last processes.

It's well established that the background gas has a strong influence on the films composition through collisional scattering effect induced by numerous collisions between the plasma species and the gas molecules or atoms. In such events, lighter plasma species diffuse to larger angles [65, 75-77]. This effect is accentuated when the mass of the light elements is lower than that of gas molecules [78]. In our case, high V/O and O_2/O mass ratios could be one reason leading to oxygen deficiency in the plasma central region and thereby in the composition of the nanoparticles grown in the gas phase and in the deposited films. Further, the backscattering effect is likely to contribute to this oxygen deficiency. According to the OES results, the heavy vanadium atoms experience a clear backscattering effect, while the backscattered light atoms of oxygen were hardly observed for the reason already explained. However, it's well known from simulation [50] and experimental [78] data, that backscattering is more intense for light elements leading, in the present case, to a still larger reduction of oxygen atoms.

3.2.2 Morphological properties

The surface morphology obtained from AFM analysis of VO_2(A) thin films is displayed in Fig. 9. The VO_2(A) films consist of assembled quasi-spherical Nps with in-plane size in the range of 40 - 70 nm giving an average size of 55 nm. This latter value is very close to the out-of-plane crystallite size calculated from XRD patterns. Also, scattered throughout the analyzed surface, large aggregates, hundreds nm in size, resulting from nanoparticle coalescence are observed. The surface roughness is about 13 nm. The variation of Nps size can find its origin in the dependence of this size on the time Nps spend in the gas phase and the region of the plume where they form. Further, the obtained compact structure with a complete substrate coverage, despite the use of high pressure, is due to the position of the substrate relative to the plume length, instead of the typical (conventional) deposition distance (few centimeters) used in PLD. At high pressure, this leads to porous [79] and fractal [80] structures.

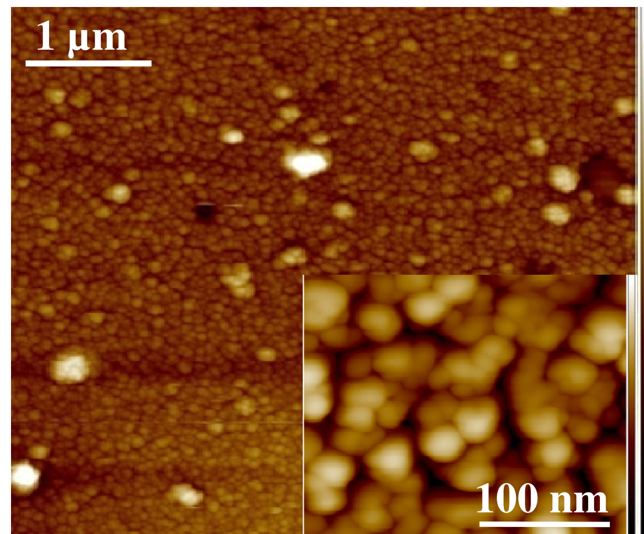

Fig. 9 AFM image of VO_2(A) nanocrystalline thin films (inset: high magnification image).

3.2.3 Optical properties

The transmittance and reflectance spectra of VO_2(A) films in the wavelength region of 250-2500 nm are shown in Fig. 10a. In the region of strong absorbance and assuming a direct transition between the valence and the conduction bands, the optical bandgap (*Eg*) was estimated using Tauc's relationship between the absorbance coefficient α and the photon energy (hv) [81]: $(\alpha hv)^2 = A(hv-E_g)$ where A is a constant. To evaluate the absorption coefficient α, the transmittance (T) and reflectance (R) data have been used in the relation: $\alpha = (1/d)\ln[(1-R)^2/T)]$, where d is the thickness of the film. In order to calculate the optical band gap energies of VO_2(A) films, a plot of $(\alpha hv)^2$ as a function of the photon energy (hv) is made. The energy gap (*Eg*) values of VO_2(A) films are determined by extrapolating the linear part of the plot relating $(\alpha hv)^2$ *vs*. (hv) to $(\alpha hv)^2=0$ (see Fig. 10b). Two linear portions were obtained giving *E*g values of 0.66 eV and 2.8 eV consistent with, respectively, intra-band and inter-band gaps transitions observed in VO_2. It was reported that VO_2(A) has V3d intra-band gap transitions from occupied *t*2g to unoccupied *t*2g orbitals in 0.5-0.7 eV range [6, 8, 9, 82]. The obtained *Eg* value of 2.8 eV corresponds to the intra-band transition from an oxygen O2*p* to unoccupied *t*2g orbitals [82].

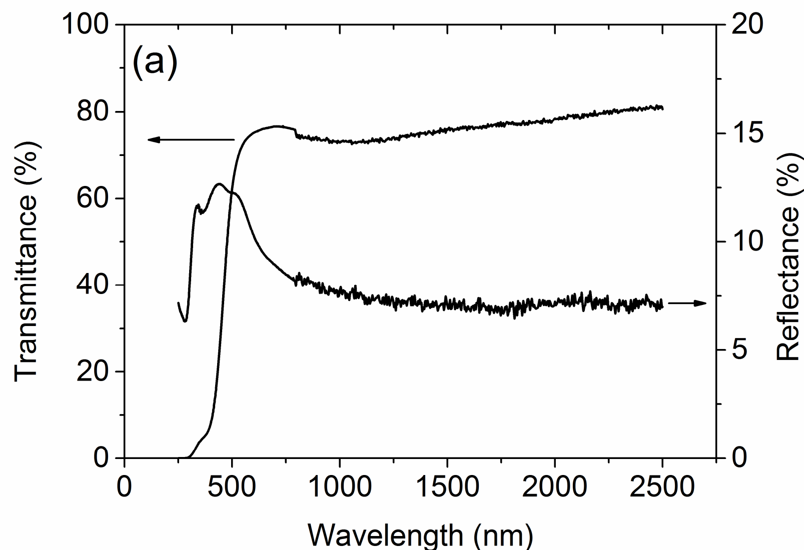

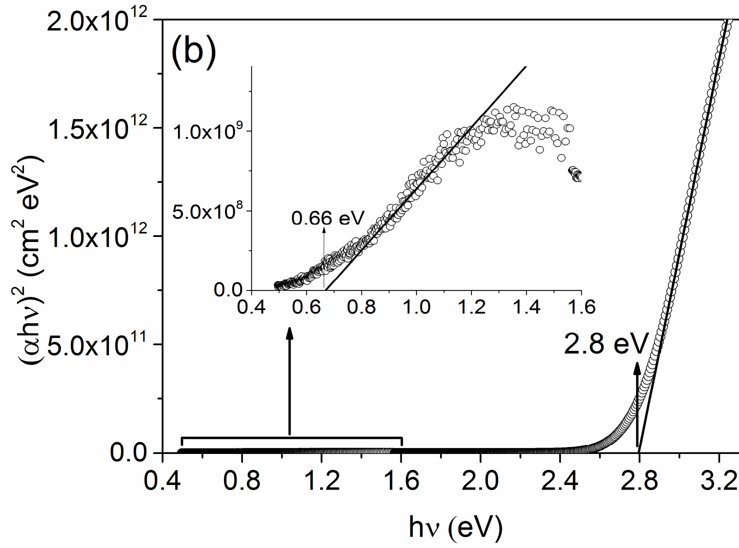

Fig. 10 a Transmittance and reflectance spectra of VO_2(A) films. **b** $(\alpha h\nu)^2$ versus energy ($h\nu$). (inset: the infrared region).

3.2.4 Electrical properties

The resistivity *vs.* temperature of VO_2(A) films displayed in Fig. 11a shows a semiconducting behavior. The resistivity drops from 12 Ωcm at room temperature to 0.17 Ωcm at 200°C. The metal-insulator transition is not observed in our VO_2(A) films which is consistent with what was reported by Srivastava *et al.* [9] for films with the same thickness. The authors considered that this result is not surprising, as even in the bulk material, the observed transition was quite weak in view of Oka *et al.* work [83]. However and more recently, Wang *et al.* [84] proved that the phase transition in VO_2(A) nanowires is a size dependent. They observed a one and a half order of magnitude jump in electrical conductivity of VO_2(A) nanowires with a large width of a μm order. Nevertheless, the phase transition is suppressed when the width of VO_2(A) nanowires is reduced to 72 nm. This later value is close to the grain size of our VO_2(A) films. This was explained in terms of finite-size effect related to the reduction of suitable nucleating defects that decreases the probability to trigger the

metal–insulator transition in the VO_2(A) nanowires with a small size [84]. This is a general rule in triggering the phase transition in VO_2 material as it has been deeply studied for the VO_2(M) phase [85].

For more details about the electrical properties, we investigated an important parameter which is the activation energy E_a of the electrical conductivity. The latter can be calculated according to Arrhenius type relation $\sigma = \sigma_0 \exp(-E_a/K_BT)$ where σ is the electrical conductivity, σ_0 is a constant, K_b is the Boltzmann's constant and T is the absolute temperature [86]. Using the resistivity *vs.* temperature curve, Ln (σ) *vs.* ($1/K_bT$) shows a linear behavior (Fig. 11b) permitting the calculation of E_a to be 0.29 eV. The latter *E*a value can be compared with the previously reported values. *E*a of the present study is very close to that reported for an individual VO_2(A) nanobelts (0.28 eV) [87] while it's much smaller than that obtained for a pressed VO_2(A) powder [83]. Further, comparing *E*a and *E*g values of our VO_2(A) films, it's clear that *E*g ≈ 2 *E*a. This indicates an intrinsic like semiconducting state of VO_2(A) nanocrystalline material.

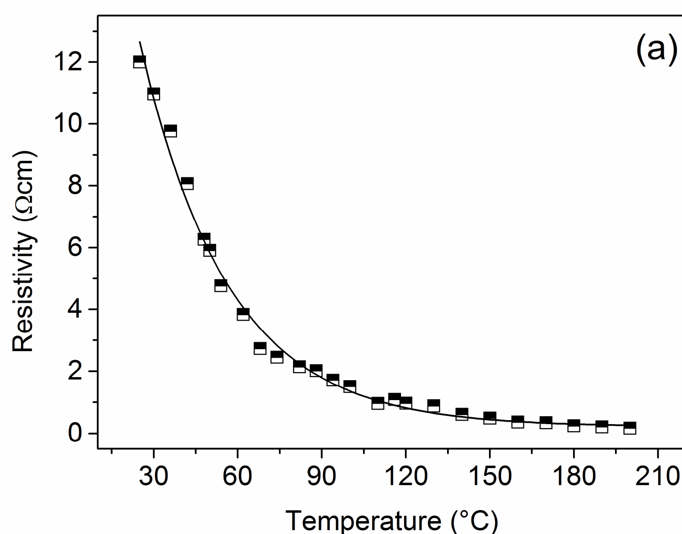

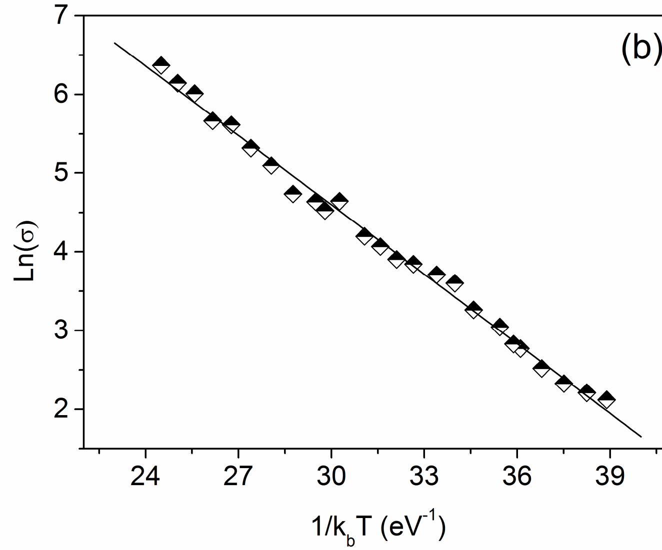

Fig. 11 Evolution of **a** the resistivity of VO_2(A) films as a function of the temperature and **b** the conductivity of VO_2(A) films as a function of (1/T).

3.2.5 Surface compositional properties

Figure 12a shows the as-measured high resolution XPS spectra of the deposited films with three intense peaks corresponding to the core level orbital of O (1s) and V ($2p_{3/2}$) and a less intense peak corresponding to the V ($2p_{1/2}$) core level orbital. After extracting the background, the O (1s) and V ($2p_{3/2}$) signals were deconvoluted and then corrected to the O (1s) (VO*x*) core level for charge referencing, taken at 530.0 eV [88]. The deconvolution of O (1s) spectrum (Fig. 12b), using Gaussian fit, reveals a sum of four peaks with binding energies associated with, double charge effect (526 eV) [89], O (1s) binding energy of the oxygen atoms in the reconstructed structures (528 eV) [90], V-O bond (530 eV) [88], and V^{5+}($2p_{3/2}$) satellite (531.37 eV) [88]. V ($2p_{3/2}$) spectrum could be fitted by three components related to V^{+2} (513.5 eV) [91], V^{+4} (516 eV) and V^{+5} (517.3 eV) [88] (Fig. 12c). The presence in the film's surface of V^{+2} and V^{+5} valence state by XPS in addition to V^{+4} valence state is inconsistent with the XRD results, which indicated the presence of only VO_2 compound, i.e., V^{+4} valence state. The presence of V^{+5} could be attributed to surface oxidation due to air

exposure [92]. V^{+2} might be produced by direct plasma deposition of VO compound. According to the OES and LP results, at the deposition distance, a part of the plasma elements preserve its atomic nature. We consider that the deposition of VO compound might be originated from this part of the plasma. As discussed above, at the distance of deposit, the plasma is rarefied in oxygen by the mechanisms given previously, but also by VO_2 nanoparticles formation (consuming more oxygen than vanadium atoms). Thus, one could suggest that the plasma in this case reaches the substrate in a state where vanadium and oxygen atoms are in a concentration balance to favor the formation of VO compound. Such complex vanadium oxidation state in VO_2 thin films was reported by Cui *et al.* [93] using depth profiling XPS analysis. In addition to V^{+4}, V^{+5} was detected at the surface of the films, while V^{+2} was detected in bulk region of the films.

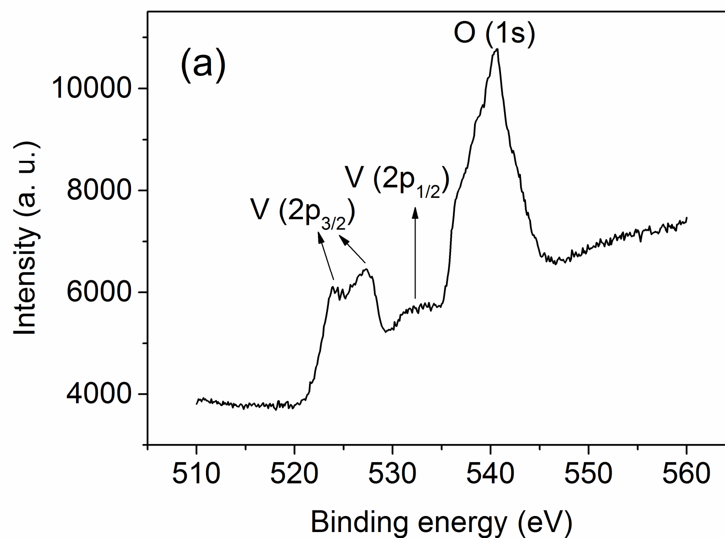

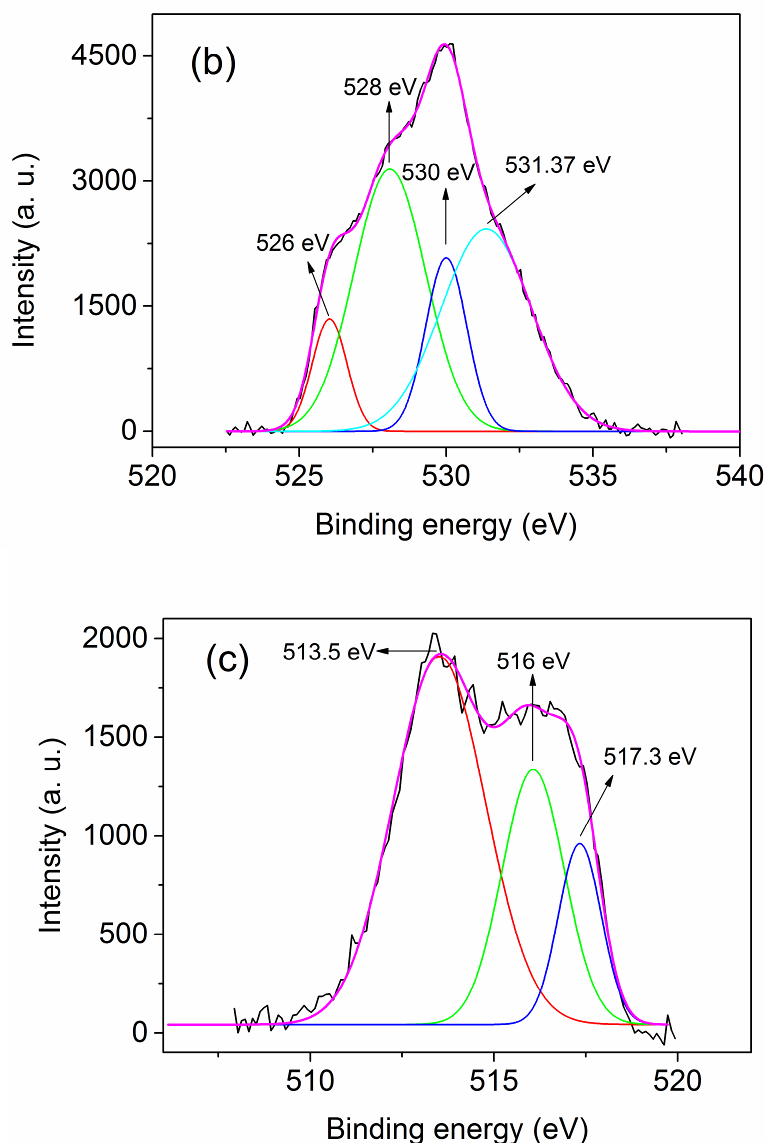

Fig. 12 a X-ray photoelectron spectra as measured (not corrected). **b** Deconvoluted and corrected O (1s) corelevel spectra after extraction the background. **c** Deconvoluted and corrected V ($2p_{3/2}$) core level spectra after extracting the background.

Finally, our achievement on room temperature synthesis of VO_2(A) Nps is of particular interest. Commonly, VO_2(A) is synthesized as elongated nanostructures [37]. Thus, thin films of VO_2(A) consisting of self-assembled Nps open new opportunities for fundamental studies and technological applications. Further, the present study paves the way to more investigations on room temperature growth of the much desired VO_2(M1) nanocrystalline thin films for nanothermochromic application. Recently, a strong

improvement in the thermochromic properties has been shown for ideal film models consisting of dispersed spheroidal VO_2 Nps, among other conditions [94, 95]. Particularly, PLD deposition process offers the opportunity to tailor the surface density and size of the nanoparticles by means of setting the position of the substrate beyond the plume length [68]. This could be a new pathway to fabricate VO_2-based nanothermochromic films consisting of self-assembled Nps on a rigid or flexible substrates for potential applications in "smart windows" for energy saving [94, 96] and sunshields for smart spacecraft thermal radiator application [19]. Even if the PLD process is disadvantaged by small area uniform coating, this could be of great benefit to exploring unique properties of nanoparticles fabricated by PLD [97].

4. Conclusion

By combining optical emission spectroscopy (OES) and Langmuir probe (LP) analysis techniques of the laser induced plasma of V_2O_5 under a typical high oxygen pressure used in pulsed laser fabrication of nanoparticles and the corresponding thin films deposition, we have clarified the plasma conditions leading to the synthesis of nanocrystalline VO_2(A) films. Plasma analysis reveals complex temporal variations in plasma dynamics as a function of the distance through the observation of four different plasma components. Three components are observed by OES where the main one undergoes a slow-down effect in juxtaposed to the second delayed forward and backscattered components. Plasma species kinetic energy and emission intensity drop to a very low level at a distance which corresponds to the visible plume length. Time of flight (TOF) signals recorded by the LP at the distance of the plume length show a much delayed fourth plasma component consisting of ionic clusters formed within the gas phase due to a high plasma confinement. This latter is regarded from the similarity of the plasma light, heavy and charged species spatio-temporal dynamics trajectories. Even though X-ray photoelectron revealed the presence of a mixed vanadium

oxide phases, the room temperature films deposited at the distance of the plume length is a judicious choice to grow highly oriented nanocrystalline vanadium dioxide thin films (A-phase) identified by means of structural, optical, electrical and compositional characterizations; at least for the oxygen pressure of 5 mbar used here. This is related to nanoparticles formation in the gas phase considering the observed ionic clusters plasma component. The obtained pure single nanocrystalline phase supports the fact that stable nanoparticles formation occurs at the distance of the plume length. Further, at this distance, we estimate a sufficient temperature, which originates from the shock wave generation in plasma-oxygen gas interface, is available to ensure the crystallinity of the nanoparticles. Finally, we consider the scattering and the back-scattering effects responsible for the nonstoichiometric transfer of the target elements to the substrate. The next research step will focus on finding the plasma conditions to grow the well desired VO_2(M1) phase at room temperature by considering distance-pressure and fluence relationship. This will only occurs by means of a combination of PLD parameters leading to a control of the plasma composition and temperature in order to pave the way for a selective growth of nanoparticles of a particular vanadium dioxide phase. This will open the way for development of low temperature innovative devices.

Acknowledgments

This work was supported by “La Direction Générale de la Recherche Scientifique et du Développement Technologique (DGRSDT)” of Algeria to whom we are grateful. The authors acknowledge Mr Hamid Menari, Mr Abdallah Trad-khodja and Mr Amine Mefoued from Semiconductor Technology Research centre (CRTSE) for respectively the optical and XPS measurements.

Compliance with ethical standards

Conflicts of interest: The authors declare no conflict of interest.

References

1. C. Lamsal, N.M. Ravindra, in Semiconductors: Synthesis, Properties and Applications, ed. By M. I. Pech-Canul, N. M. Ravindra (Springer, Switzerland, 2019), p. 127

2. M. Soltani, M. Chaker, E. Haddad, R. Kruzelecky, J. Margot, J. Vac. Sci. Technol. A 25 971 (2007)

3. S. Wang, K.A. Owusu, L. Mai, Y. Ke, Y. Zhou, P. Hu, S. Magdassi, Y. Long, Appl. Energ. 211, 200 (2018)

4. Z. Yang, C. Ko, S. Ramanathan, Ann. Rev. Mat. Res., 41, 337 (2011)

5. W. Yu, S. Li, C. Huang, Roy. Soc. Ch. Adv. 6, 7113 (2016)

6. S. Samanta, Q. Li, B. Cheng, Y. Huang, C. Pei, Q. Wang, Y. Ma, L. Wang, Phys. Rev. B 95, 045135 (2017)

7. L. Dai, Y. Gao, C. Cao, Z. Chen, H. Luo, M. Kanehira, J. Jin, Y. Liu, Roy. Soc. Ch. Adv. 2, 5265 (2012)

8. S. Lee, T.L. Meyer, C. Sohn, D. Lee, J. Nichols, D. Lee, S.S.A. Seo, J.W. Freeland, T.W. Noh, H.N. Lee, APL Mater. 3, 126109 (2015)

9. A. Srivastava, H. Rotella, S. Saha, B. Pal, G. Kalon, S. Mathew, M. Motapothula, M. Dykas, P. Yang, E. Okunishi, APL Mater. 3, 026101 (2015)

10. A. Simo, B. Mwakikunga, M. Maaza, Sensors & Transducers, 189, 143 (2015)

11. S. Lee, I.N. Ivanov, J.K. Keum, H.N. Lee, Sci. Rep. 6, 19621 (2016)

12. T.D. Vu, Z. Chen, X. Zeng, M. Jiang, S. Liu, Y. Gao, Y. Long, J. Mat. Chem. C, 7 2121 (2019)

13. S K. Shibuya, A. Sawa, AIP Adv. 5, 107118 (2015)

14. S.-Y. Li, G.A. Niklasson, C.-G. Granqvist, Thin Solid Films, 520, 3823 (2012)

15. A. Diallo, N. Ndiaye, B.D. Ngom, S. Khamlich, K. Talla, S. Ndiaye, N. Manyala, O. Nemraoui, R. Madjoe, A. Beye, J. Opt. 44, 36 (2015)

16. S. Lafane, S. Abdelli-Messaci, M. Kechouane, S. Malek, B. Guedouar, J. Lappalainen, O. Nemraoui, T. Kerdja, Thin Solid Films, 632, 119 (2017)

17. E. Gagaoudakis, G. Michail, E. Aperathitis, I. Kortidis, V. Binas, M. Panagopoulou, Y.S. Raptis, D. Tsoukalas, G. Kiriakidis, Adv. Mat. Lett. 8, 757 (2017)

18. S. Loquai, B. Baloukas, O. Zabeida, J. Klemberg-Sapieha, L. Martinu, Sol. Energ. Mat. Sol. C 155, 60 (2016)

19. M. Soltani, M. Chaker, E. Haddad, R. Kruzelesky, J. Vac. Sci. Technol. A 24, 612 (2006)

20. G. Sun, X. Cao, X. Li, S. Bao, N. Li, M. Liang, A. Gloter, H. Gu, P. Jin, Sol. Energ. Mat. Sol. C 161, 70 (2017)

21. K. Sato, H. Hoshino, M.S. Mian, K. Okimura, Thin Solid Films, 651, 91(2018)

22. P. Jin, S. Tanemura, Jpn. J. Appl. Phys. 33, 1478 (1994)

23. A. Aijaz, Y.X. Ji, J. Montero, G.A. Niklasson, C.G. Granqvist, T. Kubart, Sol. Energ. Mat. Sol. C 149, 137 (2016)

24. J.P. Fortier, B. Baloukas, O. Zabeida, J. Klemberg-Sapieha, L. Martinu, Sol. Energ. Mat. Sol. C, 125, 291 (2014)

25. M. Zhu, H. Qi, B. Wang, H. Wang, T. Guan, D. Zhang, J. Alloy. Compd. 740, 844 (2018)

26. J. Houska, D. Kolenaty, J. Vlcek, R. Cerstvy, Thin Solid Films, 660, 463 (2018)

27. M. Maaza, K. Bouziane, J. Maritz, D. McLachlan, R. Swanepool, J. Frigerio, M. Every, Opt. Mat. 15, 41 (2000)

28. E. Kumi-Barimah, D.E. Anagnostou, G. Jose, AIP Adv. 10, 065225 (2020).

29. A. De Bonis, R. Teghil, Coatings, 10, 501 (2020)

30. J. Lackner, W. Waldhauser, R. Ebner, B. Major, T. Schöberl, Surf. and Coat. Tech. 180 585 (2004)

31. T. Garcia, E. De Posada, R. Diamant, J. Peña, Appl. Phys. A 79, 919 (2004)

32. A. Mitra, R. Thareja, J. Appl. Phys. 89, 2025 (2001)

33. V. Trtik, A. Pérez, J. Navarro, C. Ferrater, F. Sánchez, M. Varela, Appl. Phys. A 69 S815 (1999)

34. T. Sasaki, S. Terauchi, N. Koshizaki, H. Umehara, Appl. Surf. Sci. 127, 398 (1998)

35. M. Ullmann, S.K. Friedlander, A. Schmidt-Ott, J. Nanopart. Res. 4, 499 (2002)

36. G.P. Johnston, R. Muenchausen, D.M. Smith, W. Fahrenholtz, S. Foltyn, J. Am. Ceram. Soc. 75, 3293 (1992)

37. M. Li, S. Magdassi, Y. Gao, Y. Long, Small, 13 1701147 (2017)

38. D. Bäuerle, in Laser Processing and Chemistry, ed. By D. Bäuerle (Springer, Berlin, 2011), p. 489

39. S. Lafane, S. Abdelli-Messaci, M. Kechouane, B.D. Ngom, S. Malek, B. Guedouar, T. Kerdja, J. Vac. Sci. Technol. A 37, 011302 (2019)

40. J. Perrièrea, E. Millonb, E. Fogarassyc, in Recent Advances in Laser Processing of Materials, ed. By J. Perrière, E. Millon and E. Fogarassy (Elsevier, Amsterdam, 2006)

41. M. Predteceensky, A. Mayorov, Appl. Supercond. 1, 2011(1993)

42. S. Lafane, T. Kerdja, S. Abdelli-Messaci, S. Malek, M. Kechouane, Appl. Phys. A 110, 241 (2013)

43. S. Amoruso, J. Schou, J.G. Lunney, Appl. Phys. A 92, 907 (2008)

44. C. Aruta, S. Amoruso, G. Ausanio, R. Bruzzese, E. Di Gennaro, M. Lanzano, F. Miletto Granozio, M. Riaz, A. Sambri, U. Scotti di Uccio, Appl. Phys. Lett. 101, 031602 (2012)

45. S. Mahmood, R.S. Rawat, Y. Wang, S. Lee, M. Zakaullah, T. Tan, S.V. Springham, P. Lee, Phys. Plasmas, 19, 103504 (2012)

46. S. Amoruso, C. Aruta, R. Bruzzese, D. Maccariello, L. Maritato, F.M. Granozio, P. Orgiani, U. Scotti di Uccio, X. Wang, J. Appl. Phys. 108, 043302 (2010)

47. H. Yousfi, S. Abdelli-Messaci, O. Ouamerali, A. Dekhira, Spectrochim. Acta B, 142, 97 (2018)

48. S. Canulescu, E. Papadopoulou, D. Anglos, T. Lippert, C. Schneider, A. Wokaun, J. Appl. Phys. 105, 063107 (2009)

49. S. Amoruso, A. Sambri, X. Wang, J. Appl. Phys. 100, 013302 (2006)

50. T. Itina, W. Marine, M. Autric, J. Appl. Phys. 82, 3536 (1997)

51. S. Amoruso, B. Toftmann, J. Schou, R. Velotta, X. Wang, Thin Solid Films, 453, 562 (2004)

52. D.H. Lowndes, D. Geohegan, A. Puretzky, D. Norton, C. Rouleau, Science, 273, 898 (1996)

53. S. Lafane, T. Kerdja, B. Ngom, S. Abdelli-Messaci, S. Malek, Appl. Surf. Sci. 269, 120 (2013)

54. B. Ngom, S. Lafane, S. Abdelli-Messaci, T. Kerdja, M. Maaza, Appl. Phys. A 122, 27 (2016)

55. S. Amoruso, R. Bruzzese, R. Velotta, N. Spinelli, M. Vitiello, X. Wang, Appl. Surf. Sci. 248, 45-49 (2005)

56. D.B. Geohegan, Thin Solid Films, 220, 138-145 (1992)

57. R. Wood, K. Chen, J. Leboeuf, A. Puretzky, D. Geohegan, Phys. Rev. Lett. 79 1571 (1997)

58. R. Wood, J. Leboeuf, D. Geohegan, A. Puretzky, K.R. Chen, Phys. Rev. B, 58, 1533 (1998)

59. A.P. French, M. Ebison, in Introduction to Classical Mechanics, ed. By A. P. French and M. G. Ebison (Springer, Dordrecht, 1986) p. 95

60. J.A. Samson, R. Cairns, J. Opt. Soc. Am. 56, 769 (1966)

61. M. Tillack, D. Blair, S. Harilal, Nanotechnology, 15, 390 (2004)

62. R. Wood, J. Leboeuf, K.R. Chen, D. Geohegan, A. Puretzky, Appl. Surf. Sci. 127, 151 (1998)

63. H.S. Kwok, H. Kim, D. Kim, W. Shen, X. Sun, R. Xiao, Appl. Surf. Sci. 109, 595 (1997)

64. S. Trusso, B. Fazio, E. Fazio, F. Neri, F. Barreca, Thin Solid Films, 518 5409 (2010)

65. J. Schou, Appl. Surf. Sci. 255 5191 (2009)

66. M. Koubaa, A. Haghiri-Gosnet, R. Desfeux, P. Lecoeur, W. Prellier, B. Mercey, J. Appl. Phys. 93 5227 (2003)

67. D. Dellasega, A. Facibeni, F. Di Fonzo, V. Russo, C. Conti, C. Ducati, C.S. Casari, A.L. Bassi, C.E. Bottani, Appl. Surf. Sci. 255, 5248 (2009)

68. D.H. Lowndes, C.M. Rouleau, T. Thundat, G. Duscher, E. Kenik, S. Pennycook, J. Mater. Res. 14, 359 (1999)

69. P.N. Barnes, P.T. Murray, T. Haugan, R. Rogow, G.P. Perram, Physica C, 377, 578 (2002)

70. J S. Ji, Y. Zhao, F. Zhang, P. Jin, J. Ceram. Soc. Jpn.118, 867 (2010)

71. S. Luo, W.A. Daoud, Materials, 9, 123 (2016)

72. B.D. Cullity, Elements of X-ray Diffraction (Addison-Wesley Publishing, Reading Massachusetts, 1956)

73. P. Dyer, A. Issa, P. Key, Appl. Phys. Lett. 57, 186 (1990)

74. R.L. Sproull, Modern Physics, John Wiley & Sons, New York, 1966

75. S. Wicklein, A. Sambri, S. Amoruso, X. Wang, R. Bruzzese, A. Koehl, R. Dittmann, Appl. Phys. Lett. 101, 131601 (2012)

76. I. Konomi, T. Motohiro, M. Horii, M. Kawasumi, J. Vac. Sci. Technol. A 26 1455 (2008)

77. J. Gonzalo, C. Afonso, J. Perriere, R.G. San Roman, Appl. Surf. Sci. 96, 693 (1996)

78. S. Amoruso, in Metal Oxide-Based Thin Film Structures, ed. By N. Pryds, V. Esposito (Elsevier, Amsterdam, 2018) p. 133

79. S. Mohanty, P. Lee, T. Tan, S. Springham, A. Patran, R. Ramanujan, R. Rawat, Appl. Surf. Sci. 252, 2806 (2006)

80. A. Maffini, A. Pazzaglia, D. Dellasega, V. Russo, M. Passoni, Phys. Rev. Mat. 3, 083404 (2019)

81. J. Tauc, A. Menth, States in the gap, J. Non-Cryst. solids, 8, 569 (1972)

82. S. Choi, S.J. Chang, J. Oh, J.H. Jang, S. Lee, Adv. Electron. Mater. 4, 1700620 (2018)

83. Y. Oka, T. Ohtani, N. Yamamoto, T. Takada, J. Ceram. Soc. Jpn. 97, 1134 (1130)

84. C.Q. Wang, J. Shao, X.L. Liu, Y. Chen, W.M. Xiong, X.Y. Zhang, Y. Zheng, Phys. Chem. Chem. Phys. 18, 10262 (2016)

85. R. Lopez, T. Haynes, L. Boatner, L. Feldman, R.F. Haglund Jr. Phys. Rev. B 65, 224113 (2002)

86. X. Zhong, X. Zhang, A. Gupta, P. LeClair, J. Appl. Phys. 110, 084516 (2011)

87. M. Li, F. Kong, L. Li, Y. Zhang, L. Chen, W. Yan, G. Li, Dalton T. 40, 10961 (2011)

88. G. Silversmit, D. Depla, H. Poelman, G.B. Marin, R.D. Gryse, J. Electron Spectrosc. 135, 167 (2004)

89. A.V. Fetisov, G.A. Kozhina, S.Kh. Estemirova, V.B. Fetisov, R.I. Gulyaeva, Physica C, 508, 62 (2015)

90. S. Gunther, S. Bocklein, J. Wintterlin, M.A. Nino, T.O. Mentes, A. Locatelli, Chem. Cat. Chem. 5, 3342 (2013)

91. C.N.R. Rao, D.D. Sarma, S. Vasudevan, M.S. Hegde, Proc. R. Soc. Lond. A 367, 239 (1979)

92. Y. Li, J. Liu, D. Wang, G. Pan, Mater. Res. Bull. 100, 220 (2018)

93. Y. Cui, X. Wang, Y. Zhou, R. Gordon, S. Ramanathan, J. Cryst. Growth, 338, 96 (2012)

94. S.Y. Li, G.A. Niklasson, C.-G. Granqvist, J. Appl. Phys. 108, 063525 (2010)

95. J. Zhu, Y. Zhou, B. Wang, J. Zheng, S. Ji, H. Yao, H. Luo, P. Jin, ACS Appl. Mater. Interfaces, 7, 27796 (2015)

96. H. Kim, Y. Kim, K.S. Kim, H.Y. Jeong, A.-R. Jang, S.H. Han, D.H. Yoon, K.S. Suh, H.S. Shin, T. Kim, ACS Nano, 7, 5769 (2013)

97. M. Kim, S. Osone, T. Kim, H. Higashi, T. Seto, KONA Powder and Part. J. 34, 80 (2017)